Article publicat / *Published paper*:

Arias, A., Caum, J., Griñó, R. Moving towards the maximum speed in stepping motors by means of enlarging the bandwidth of the current controller. "Mechatronics", December 2016, p. 51-62. DOI: http://dx.doi.org/10.1016/j.mechatronics.2016.10.018

Contents lists available at ScienceDirect

Mechatronics

journal homepage: www.elsevier.com

Moving towards the maximum speed in stepping motors by means of enlarging the bandwidth of the current controller

Antoni Arias [a,*], Jesús Caum [b], Robert Griñó [a]

[a] Institute of Industrial and Control Engineering, Universitat Politècnica de Catalunya, Diagonal 647, 08028, Barcelona, Catalonia, Spain
[b] Centre for Sensors, Instruments and Systems Development Universitat Politècnica de Catalunya, Rambla de Sant Nebridi, 10, 08222, Terrassa, Catalonia, Spain

ARTICLE INFO

Article history:
Received 6 May 2016
Received in revised form 20 September 2016
Accepted 24 October 2016
Available online xxx

Keywords:
Stepping motors
Rapid-response manufacturing
Mechatronics
Current controller bandwidth
Maximum speed
PCB

ABSTRACT

This paper pursues to maximise the mechanical speed when using stepping motors (SM) without position sensors in order to achieve a rapid-response manufacturing whenever any equipment based on such electrical machines is involved.

The novelty of this paper is the fact that not only the bandwidth of the current controllers is improved for such maximization of the SM mechanical speed, as traditionally done in previous works, but also a comprehensive approach has been addressed. Such global approach starts justifying why the traditional PI controller is not sufficient and it includes the analytical tuning of the current controllers, considering implementation tiny issues (but of paramount importance) such as the delays caused by the processor and the sample and hold current measurements. It is proved and justified that this previously mentioned issues, which are often omitted, play a crucial role when trying to maximise the speed of the SM, since the electrical fundamental frequencies of the SM move close to the sampling frequency. Therefore, the analytical process to tune and implement the current controllers will have to be done in discrete-time domain, i.e. using the Z transform and treating the SM drive as a sampled data system.

Experimental waveforms and results based on real prototypes will prove the validity of the entire research.

Finally, a real case-study based on Printed Circuit Board (PCB) prototyping machine which is composed by two stepper machines, is fully reported. Such PCB prototype is the fruitful collaboration between the University (research institution) and a private company (industry).

1. Introduction

Stepping or stepper motors (SMs) are extensively used in position controlled drives in a wide range of applications, from traditional drives [1,2], up to state of the art applications [3–6]. In [3], an automatic ultrasound scanning system uses an SM to accurately position the planar piston transducer and the needle-type hydro-phone in the tank. In [4], the authors point out that the SM is a satisfactory choice for driving the control rods in a modular high temperature gas-cooled reactor. The state of the art Π-joint lab prototype presented in [5] uses a miniature hybrid SM as a linear actuator, while in [6] a new type of a linear stepper drive for sensorless positioning tasks in hydraulics is reported.

Despite some Field Oriented Controllers [7] with position feedback are reported [8,9], the SM major advantage is the capability to perform control position without the need of any electromechanical sensor to measure the position. Such inherent open-loop control position capability is based on the fact that this electrical machine is able to be driven in a step-by-step algorithm. Furthermore, the micro stepping technique, which divides each step in many incremental parts surpasses the discretization of the steps and allows an almost continuous position control [1,2]. Such stepping open-loop position control is reliable as long as the machine does not lose synchronisation and does not miss any step. Research efforts are driven in [10] and [11] to detect step-outs and compensate for them to keep the accuracy in the position control. Also, more traditional sensorless control approaches have been carried out based on extended Kalman filters [12,13] and passive nonlinear [14–16] as well as disturbance [17] observers.

Still, SMs have torque and speed ripples problems which have driven the research attention [18–20] sometimes even using artificial intelligent techniques such as neural networks [21,22].

This paper pursues to maximise the SM mechanical speed in order to achieve a rapid-response manufacturing. Many high-precision motion systems [23] are designed in the continuous s domain, which is a handicap when facing high speeds. The three highest maximum speeds reported in the previously cited works are 288 rpm for [11], 380 rpm for [12] and 450 rpm for [22], whereas in this paper 1320 rpm is the highest maximum speed reported. To achieve such goal, firstly, the need of surpassing the widely used traditional proportional and integral (PI) controller [24,25] is justified and secondly, a new second-order controller is designed and tuned in z domain, which brings the possibility to properly compensate the processing delays as well as the pulse width modulation (PWM) of the power electronics actuator. Such proposed high bandwidth (BW) controller has envisaged, from the very beginning, the industrial feasibility for further commercialization. Therefore, the proposed algorithm not only has the possibility to be implemented in cheap microcontrollers but also it is fully understandable attending the classic control theory,

* Corresponding author. Fax. +34937398016.
Email address: antoni.arias@upc.edu (A. Arias)

http://dx.doi.org/10.1016/j.mechatronics.2016.10.018
0957-4158/

likewise the well-known PI controller, which is always a plus when dealing with industry and practical engineers.

Lastly, a real prototype designed for such research is fully described and high speed results are reported.

Considering that the proposed controller is somehow competing with the well-known and widely used PIs, an extensive experimental comparison with the mentioned PIs controllers is illustrated.

To conclude the work, a 2 axis rapid prototyping Printed Circuit Boards (PCBs) machine [26], which has two stepper motors axis, is fully reported. Such PCB machine is the fruitful collaboration between the University and a private company and it is a tangible example of how increasing the SM speed reduces the time employed for rapid prototyping applications. The PCB manufacturing is an emblematic example of the nowadays electronics industry [27,28].

2. Stepper motor model

SMs have two phases (labelled α and β) in quadrature, whose electrical equations are represented in (1) and (2).

$$\frac{di_\alpha}{dt} = \frac{1}{L}\left(v_\alpha - Ri_\alpha + \omega_m \psi_{PM} N_r \sin\left(N_r \omega_m t\right)\right) \tag{1}$$

$$\frac{di_\beta}{dt} = \frac{1}{L}\left(v_\beta - Ri_\beta + \omega_m \psi_{PM} N_r \sin\left(N_r \omega_m t - \pi/2\right)\right) \tag{2}$$

The torque production, whose mathematical expression is given in (3), is achieved, as in the majority of electrical machines, by the interaction (or vector product) between the magnetic flux and the current.

$$T_e = N_r \psi_{PM} \sin\left(N_r \omega_m t + \pi/2\right)\ i_\beta - N_r \psi_{PM} \sin\left(N_r \omega_m t\right)\ i_\alpha \tag{3}$$

Finally the mechanical speed is given in (4), which models a first order mechanical system with an external load torque

$$\frac{d\omega_m}{dt} = \frac{1}{J}\left(T_e - T_L - F\omega_m\right) \tag{4}$$

In order to guarantee the proper micro stepping functionality, a closed-loop current controller (with current sensors) must be performed. Despite the only references are the alpha and beta currents, the position set point is indirectly given within the angle included by the mentioned current references, which are sinusoidal. Therefore, the success of the position control depends entirely on the sinusoidal current tracking capability and, consequently, on the current controller performance.

From (1) and (2) it is concluded that the plant dynamics can be simplified to a first order system composed by the resistance and the inductance. The third term corresponds to back electromotive force (*EMF*) and it can be modelled as a disturbance. Fig. 1 shows the general block diagram.

Due to the nature of the SM, the typical number of rotor slots is 50, which implies that the electrical angular speed is 50 times larger than the mechanical one. This multiplying factor is the main challenge when maximising the mechanical speed. For instance, for achieving an angular speed of 500 rpm (≈57,36 rad/s, 8,33 Hz) a sinusoidal current waveform of 25.000 rpm (≈2618 rad/s, 416 Hz) is needed, which clearly compromises the BW of the current controller.

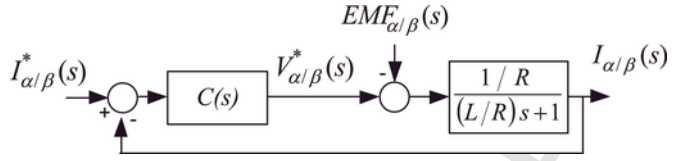

Fig. 1. Control scheme with the controller C(s), plant transfer function and the current, voltage and back EMF signals for the alpha and beta phases.

Research efforts have been made to design the controller (*C(s)*) not only to guarantee the stability but also to maximise the tracking capability of this current closed-loop control at such high angular speeds [29].

3. Traditional PI control approach. System_1 and System_2

Traditionally the current controllers for electric machines are addressed tuning a proportional and integral (PI) controller in Laplace (s) domain, as it is shown in Fig. 2, to fulfil the desired specifications. The pre filter (PF), PI and the plant transfer function (G(s)) are given in Eqs. (5), (6) and (7) respectively.

$$PF(s) = \frac{1}{\left(K_P/K_I\right)\ s+1} \tag{5}$$

$$PI(s) = K_P + \frac{K_I}{s} = K_I \frac{\left(K_P/K_I\right)\ s+1}{s} \tag{6}$$

$$G(s) = \frac{1/R}{(L/R)\ s+1} \tag{7}$$

The closed-loop system transfer function can be expressed as indicated in (8)

$$\frac{I(s)}{I^*_{PF}(s)} = \left(K_I/L\right) \frac{\left(K_P/K_I\right) s+1}{s^2 + s\left(R+K_P\right)/L + K_I/L} \tag{8}$$

By means of the unity-gain PF given in (5) and provided that (K_P / K_I) > *0*, the unwanted zero is cancelled and therefore Eq. (8) is reduced to a second-order system, whose generic transfer function is equal to:

$$\frac{\omega_n^2}{s^2 + 2\xi\omega_n \cdot s + \omega_n^2} \tag{9}$$

The PI will be tuned using Eqs. (10) and (11), to fulfil the specifications of settling time at 2% ($Ts_{2\%}$), given in Eq. (12) and damping factor (ζ), which will be fixed to ζ = 0.7071 in order to keep the overshoot to less than 4.3% and therefore to avoid the resonance peak in the gain of the closed-loop frequency response. On the other hand,

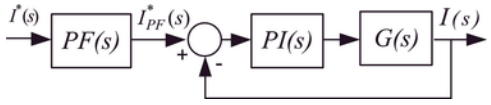

Fig. 2. Current control loop with a PI controller and a PF. System_1.

the $Ts_{2\%}$ will be minimised in order to increase the current closed-loop BW and, therefore, maximise the maximum mechanical speed.

$$K_I = \frac{4.22^2 \cdot L}{\zeta^2 \cdot Ts_{2\%}^2} \tag{10}$$

$$K_P = \frac{2 \cdot 4.22 \cdot L}{Ts_{2\%}} - R \tag{11}$$

$$Ts_{2\%} = \frac{4.22}{\zeta \cdot \omega_n} \;\rightarrow\; \omega_n = \frac{4.22}{\zeta \cdot Ts_{2\%}} \tag{12}$$

In order to implement it digitally (i.e. in a microcontroller or a in a digital signal processor (DSP)), the traditional approach, valid for the majority of electric machines drives [7], consists in using the Euler rectangular, either forward or backward, approximation given in Eqs. (13a) and (13b) respectively.

$$\frac{1}{s} = T\frac{1}{z-1} \tag{13a}$$

$$\frac{1}{s} = T\frac{z}{z-1} \tag{13b}$$

The Euler discretized current control loop is no longer represented by Fig. 2 and its new block diagram is illustrated in Fig. 3:

The well-known zero-order hold (ZOH) transformation method [30] has been used to obtain the plant transfer function in z domain according to expression (14).

$$G(z) = \left(1 - z^{-1}\right)\; Z\left\{\frac{G(s)}{s}\right\} \tag{14}$$

The new PF_i and PI_i controller transfer functions are given in expressions (15) and (16), where versions (a) and (b) stand for the forward (f) and backward (b) Euler approximations, respectively.

$$\mathrm{PF_f}(z) = \frac{1}{\left(K_P/K_I\right)\frac{z-1}{T} + 1} = \frac{1}{\frac{K_P}{K_I T}z + 1 - \frac{K_P}{K_I T}} \tag{15a}$$

$$\mathrm{PF_b}(z) = \frac{1}{\left(K_P/K_I\right)\frac{z-1}{Tz} + 1} = \frac{z}{\left(\frac{K_P}{K_I T} + 1\right)z - \frac{K_P}{K_I T}} \tag{15b}$$

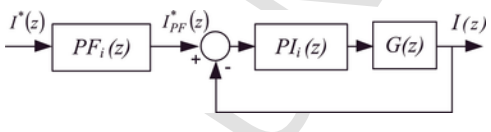

Fig. 3. Current control loop with the Euler discretized PI_i and PF_i controllers, where i = (f, b) stands for the forward and backwards Euler approximations. System_2.

$$\mathrm{PI_f}(z) = K_P + K_I T\frac{1}{z-1} = \frac{K_P z + K_I T - K_P}{z-1} \tag{16a}$$

$$\mathrm{PI_b}(z) = K_P + K_I T\frac{z}{z-1} = \frac{\left(K_P + K_I T\right)z - K_P}{z-1} \tag{16b}$$

As a matter of example, Table 1 and Table 2 compare the closed-loop poles, the PF poles and the BW of both systems for two different $Ts_{2\%}$ values and always for a $T = 50$ μs and $\zeta = 0.7071$. When the closed-loop BW is far from $F_S/2$, as in the case of Table 1, the Euler's approximation is good enough and the error introduced is almost imperceptible. On the contrary, when the closed-loop BW is increased to achieve high speeds, the closed-loop poles differ from the targeted place and eventually they may lay outside the unit circle in the z-plane and therefore the system might become unstable. Table 2 shows the data for this later case, where the System_2 closed poles are outside the unit circle.

To conclude, it has to be pointed out that this traditional approach, which is widely used for other types of electrical machines, is not suitable for the SM. A first reason is the fact that a regulation oriented controller is not enough and it is needed a sinusoidal tracking regulator. In other words, because the Park transformation cannot be applied for the lack of position information, the closed-loop system must track a sinusoidal reference, instead of just a step. The second reason is the error introduced by the Euler's approximation when the closed-loop system BW gets closer to the $F_S/2$, (which is rather the case when dealing with SM with a factor of 50 between the mechanical and the electrical angular frequencies).

Table 1
Closed loop poles, PF pole and BW when $Ts_{2\%} = 5$ ms.

System / description	Closed loop poles	PF pole	BW Hz
System_1 / Ideal continuous	−844 +/− 844i	−1018	189
System_2(a) / forward Euler	0.958 +/− 0.042i	0.949	198
System_2(b) / backward Euler	0.956 +/− 0.04i	0.952	189

Table 2
Closed loop poles, PF pole and BW when $Ts_{2\%}$ = 200 μs.

System/description	Closed loop poles	Non cancelled zeros	PF poles	Overall BW Hz
System_1/Ideal continuous	−21,100 +/− 21100i	None	−21,200	4743.3
System_2(a)/forward Euler	−0.0474 +/− 1.05i	None	0.0623	***Unstable***
System_2(b)/backward Euler	−0.404	None	0.485	***Unstable***
System_3/PI(Z) tuned. No delays in the plant	− 2.71 0.17 +/− 0.3i	None	0.52	6100.8
System_4/3 PI(Z). Delay in the plant.	0.404 0.37 +/− 0.959i	−0.993	0.52	***Unstable***
System_5/PI(Z) tuned with delay	1.71 0.17 +/− 0.3i	−0.993	−3.05	***Unstable***
System_6/New controller	0.17 +/− 0.3i −0.06 +/− 0.1i	−0.993	0.594 0.0028	4766

The rational next step is to tune all controllers directly in z domain, i.e. to do a direct digital design.

4. PI controller tuned in z domain. System_3 and System_4

The new scheme, labelled as System_3, is illustrated in Fig. 4, and its characteristic equation is given in (17). Using backward or forward PI transfer function will make no difference since the constants will take the necessary values to always end up with the same controller and therefore the same closed-loop system.

$$1 + PI(z)\cdot G(z) = 0$$
$$1 + \frac{K_P\, z - K_P + K_I T}{z-1}\,\frac{1}{R}\,\frac{1-e^{-\frac{R}{L}T}}{z-e^{-\frac{R}{L}T}} = 0 \tag{17}$$

Provided that the specifications are still the same, settling time ($Ts_{2\%}$) as given in Eq. (12) and damping factor (ζ), the desired closed-loop characteristic equation is:

$$z^2 - 2e^{\left(-\frac{4.22\cdot T}{Ts_{2\%}}\right)}\cdot\cos\left(\frac{4.22\sqrt{1-\xi^2}\cdot T}{Ts_{2\%}\cdot\zeta}\right)\cdot z + e^{\left(-\frac{2\cdot 4.22\cdot T}{Ts_{2\%}}\right)} = 0 \tag{18}$$

From Eqs. (17) and (18), the PI controller will be tuned according to expressions (19) and (20)

$$K_P = \frac{-2e^{-\frac{4.22\cdot T}{Ts_{2\%}}}\cdot\cos\left(\frac{4.22\sqrt{1-\xi^2}\cdot T}{Ts_{2\%}\cdot\zeta}\right) + 1 + e^{-\frac{R}{L}T}}{1-e^{-\frac{R}{L}T}}R \tag{19}$$

$$K_I T = \frac{e^{-2\frac{4.22}{Ts_{2\%}}T} - e^{-\frac{R}{L}T}}{1-e^{-\frac{R}{L}T}}R + K_P \tag{20}$$

Despite the fact that in simulation this approach performs as intended, once it is implemented it underperforms and eventually, when increasing the BW, it may become unstable. The reason for this is the fact that the delays are neither modelled nor considered when designing and tuning the PI controller. Actually this approach is unrealistic; however it can work properly when the BW is low.

The real system, labelled as System_4, is the one composed by this PI together with the delays. In Table 2 it can be seen how System_4 has its closed-loop poles in the unstable region, while the ideal and unrealistic System_3 fulfils the specifications.

5. Modelling the delays. System_5

The delays are mainly caused by the time needed by the DSP to sample the currents and execute the controllers as well as the PWM unit to synthetize the required voltage. In this work such delay has been reduced from the typical one sample time (z^{-1}) to just a portion (m) of it (z^{-1+m}). However, the Z transform is defined for an entire number of delays, not for a fractional portion of them. Therefore, the modified Z transform (Z_m) [30] needs to be used to model such fractional part of the sampling time delay as shown in Fig. 5.

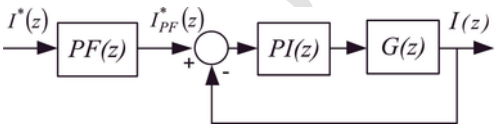

Fig. 4. Current control loop with the PI and PF controllers already tuned in z domain. System_3.

The new characteristic equation is given in (21) and its equivalent polynomial form in (22).

$$1 + \frac{K_P\, z + K_I T - K_P}{z-1}\,\frac{\left(1-e^{-\frac{R}{L}mT}\right)z + e^{-\frac{R}{L}mT} - e^{-\frac{R}{L}T}}{Rz\left(z-e^{-\frac{R}{L}T}\right)} = 0 \tag{21}$$

$$\begin{aligned} &z^3 + z^2\left(-1 - e^{-\frac{R}{L}T} + \frac{K_P}{R}\left(1-e^{-\frac{R}{L}mT}\right)\right) \\ &+z\left(e^{-\frac{R}{L}T} + \frac{K_P}{R}\left(e^{-\frac{R}{L}mT} - e^{-\frac{R}{L}T}\right) + \frac{K_I T - K_P}{R}\left(1-e^{-\frac{R}{L}mT}\right)\right) \\ &+\left(\frac{K_I T - K_P}{R}\left(e^{-\frac{R}{L}mT} - e^{-\frac{R}{L}T}\right)\right) = 0 \end{aligned} \tag{22}$$

From (22) it is clear that the new closed-loop system will now have three poles; the targeted two poles from (18) plus an extra third pole labeled as "c" in (23).

$$\begin{aligned} &\left(z^2 - 2e^{\left(-\frac{4.22\cdot T}{Ts_{2\%}}\right)}\cos\left(\frac{4.22\sqrt{1-\xi^2}\cdot T}{Ts_{2\%}\cdot\zeta}\right)z\right. \\ &\left.+\,e^{\left(-\frac{2\cdot 4.22\cdot T}{Ts_{2\%}}\right)}\right)(z-c) = 0 \end{aligned} \tag{23}$$

The new wanted polynomial expression is given in (24)

$$\begin{aligned} &z^3 + z^2\left(-2e^{\left(-\frac{4.22\cdot T}{Ts_{2\%}}\right)}\cos\left(\frac{4.22\sqrt{1-\xi^2}\cdot T}{Ts_{2\%}\cdot\zeta}\right) - c\right) \\ &+z\left(e^{\left(-\frac{2\cdot 4.22\cdot T}{Ts_{2\%}}\right)} - 2c\,e^{\left(-\frac{4.22\cdot T}{Ts_{2\%}}\right)}\cos\left(\frac{4.22\sqrt{1-\xi^2}\cdot T}{Ts_{2\%}\cdot\zeta}\right)\right) - c\,e^{\left(-\frac{2\cdot 4.22\cdot T}{Ts_{2\%}}\right)} = 0 \end{aligned}$$

According to the control theory [31,32], in order to place the closed-loop poles in any desired place, the controller must have a number of coefficients equal to the number of the closed-loop poles. Therefore, a PI with just two coefficients is not enough. The mathe-

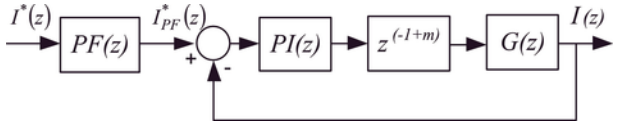

Fig. 5. Current control loop with the PI and PF controllers already tuned in z domain. A delay smaller than the sampling time has been modeled by means of the modified Z transform. System_5.

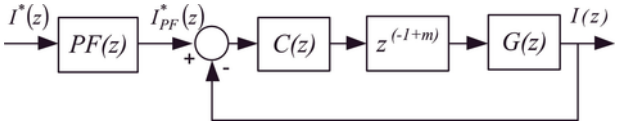

Fig. 6. Current control loop with the C and PF controllers already tuned in z domain. A delay smaller than the sampling time has been modeled by means of the modified Z transform. System_6.

matical solution to impose the desired closed-loop poles, might eventually bring the third pole of the system outside the stable region (1,71 + 0i) when maximising the BW, as it is indicated in Table 2.

6. New controller. System_6

As it has been mentioned before, and in order to fulfil the control theory, the new controller must possess a number of coefficients equal to the number of closed-loop poles. Moreover, the integral action is required to guarantee the regulation capability (zero error in steady state in front of a step reference). Also, the controller must be causal and therefore the order of the controller denominator has to be increased. The proposed controller and the new characteristic equation are given in (25) and (26) respectively.

$$C(z) = \frac{b_2 z^2 + b_1 z + b_0}{(z - a_0)(z - 1)} \tag{25}$$

$$1 + \frac{b_2 z^2 + b_1 z + b_0}{(z - a_0)(z - 1)} \frac{\left(1 - e^{-\frac{R}{L}mT}\right) z + e^{-\frac{R}{L}mT} - e^{-\frac{R}{L}T}}{Rz\left(z - e^{-\frac{R}{L}T}\right)} = 0 \tag{26}$$

From (26), it can be seen that the closed-loop system has four poles but the controller possesses also the same number of coefficients.

The specifications will then be the closed-loop poles positions. Two of them to fulfil the wanted dynamics pointed out in (18) and the other two will be placed to possess the maximum dynamics, i.e. its $T_{s2\%}$ will be twice the sampling time and its damping factor equal to 0.7071. Hence, the targeted characteristic equation will be:

$$\left(z^2 - 2e^{\left(-\frac{4.22 \cdot T}{T s_{2\%}}\right)} \cdot \cos\left(\frac{4.22\sqrt{1-\xi^2} \cdot T}{T s_{2\%} \cdot \zeta}\right) \cdot z + e^{\left(-\frac{2 \cdot 4.22 \cdot T}{T s_{2\%}}\right)}\right) \times \left(z^2 - 2e^{-2.11} \cdot \cos(2.11) \cdot z + e^{-4.22}\right) = 0 \tag{27}$$

Imposing the characteristic Eq. (26) and the specifications (27) to be the same, the four coefficients a_0, b_2, b_1 and b_0 are found.

Once the controller is properly designed, stable and fulfilling the required dynamics, the PF needs to be designed in order to cancel the undesired influence of the existing closed-loop zeros. The closed-loop numerator is given in (28) and it contains three zeros, two from the controller and a third one from the plant itself.

$$\frac{1 - e^{-\frac{R}{L}mT}}{R} \left(b_2 z^2 + b_1 z + b_0\right) \left(z + \frac{e^{-\frac{R}{L}mT} - e^{-\frac{R}{L}T}}{1 - e^{-\frac{R}{L}mT}}\right) \tag{28}$$

The zero from the plant might be very close to the unity circle. Actually, for the data given in Table 2, this zero takes the value (−0.993 + 0i). Therefore, if the PF includes such pole, it would introduce a very slow oscillating dynamics which would worsen the overall response. Therefore, the feasible PF, whose transfer function is given in (29) and has a unity gain, will just cancel the two zeros introduced by the controller.

$$\frac{b_2 + b_1 + b_0}{b_2 z^2 + b_1 z + b_0} \tag{29}$$

7. Implementation and workbench

For the real implementation, the voltage demand must be saturated in order to protect the whole drive. Therefore, the integrator part must contain an anti-windup [33,34] strategy. Hence, the proposed controller must be split to isolate the integral part according to (30). The adopted anti-windup strategy is detailed in Fig. 7.

$$\frac{b_2 z^2 + b_1 z + b_0}{(z - a_0)(z - 1)} = \frac{A}{z - 1} + \frac{B}{z - a_0} + b_2 \tag{30}$$

Eqs. (31) and (32) show the new coefficients

$$A = b_1 + b_2(a_0 + 1) - \frac{b_0 + a_0(a_0 b_2 + b_1)}{a_0 - 1} \tag{31}$$

$$B = \frac{b_0 + a_0(a_0 b_2 + b_1)}{a_0 - 1} \tag{32}$$

The floating point digital signal controller used is the Texas Instruments TMS320F28335 at 150 MHz [35], which (i) minimizes any numerical problem when executing the controllers and (ii) achieves low sampling time (50 μs in this work). It contains also the required PWM units and analogue to digital converters (ADC) with a conversion time of 6.67 ns and 12 bits.

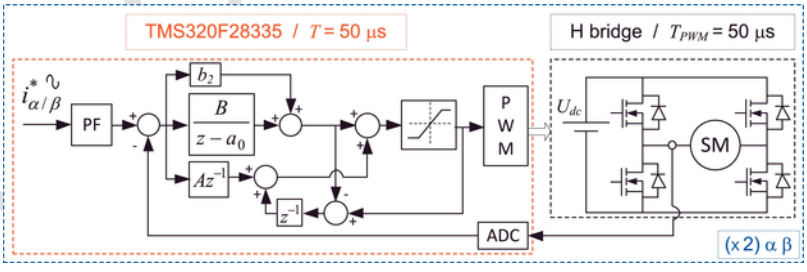

Fig. 7. Current control with the saturation and anti-windup, H-bridge power converter and SM detailed scheme. There are two identical schemes for the alpha and beta SM phases.

Two identical power converters, whose specific semiconductors data are detailed in Table 3, have been used for the alpha and beta phases, based on the well-known H-bridge topology, as Fig. 7 illustrates. The PWM strategy used is based on the well-known unipolar one, fully described in [36], and the sampling time of the whole controller, which is the same as the PWM period, has been set to 50 μs.

The current references are obtained from either a position or speed set point, as it is illustrated in Fig. 8.

Fig. 9 is a picture of the workbench composed by the SM, an encoder and a DC machine in order to create an external load torque. Also the DSP board and the power unit are illustrated. Such workbench has been firstly used to corroborate the proper functionality of the new algorithms prior to being implemented in a real industrial drive.

8. Experimental results

In order to corroborate the SM current control algorithm and prove its tracking capability at high speeds, three sets of experimental results have been carried out. Hence, current, speed and position waveforms in front of (i) speed steps, (ii) speed reversal trapezoidal profile and (iii) constant speed with load impact, have been carried out.

For the speed steps and speed reversal trapezoidal profiles, a comparison to prove the superiority of the new controller has been addressed. The systems under comparison are the PI and the new controller, previously named as System_5 and System_6, respectively. The closed-loop poles have been placed to enlarge the most the closed-loop BW, keeping the closed-loop system stable. Hence, the settling time is 400 μs ($Ts_{2\%}$ = 400 μs) and 200 μs ($Ts_{2\%}$ = 200 μs) for System_5 and System_6, respectively.

System_5 (blue trace) and System_6 (red trace) closed-loop frequency response including the pertinent PF are plotted in Fig 10, where it is clearly illustrated how System_6 has a larger BW.

Fig. 11 plots System_5 (blue trace) and System_6 (red trace) frequency response in front of a perturbation. As a matter of example, the back EMF sinusoidal perturbation, will have a rejection of −24.6 dB and −36.4 dB at 1 kHz for systems 5 and 6, respectively.

Table 3
Stepper motor and H bridge converter characteristics.

Stepper Motor IGUS 56 (NEMA23)		
Maximum voltage (DC)		60 V
Nominal voltage (DC) / current		48 V/4.2 A
Holding/detent torque		2.0 Nm/0.068 Nm
R / L		0.5 Ω/1.9 mH
Step angle / Nr		1.8º / 50
Power MOSFET IRF540N		
V_{DSS} = 100 V	I_D = 33 A	$R_{DS(on)}$ = 44 mΩ
Other parameters		
U_{dc} = 100 V	$T = T_{PWM}$ = 50 μs	

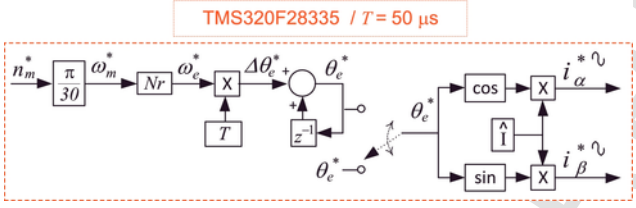

Fig. 8. Current references generation block. The electrical angle is given by either the speed or position set point.

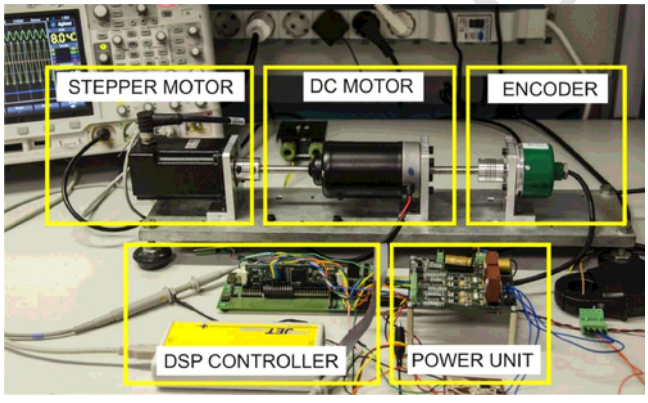

Fig. 9. Test workbench composed by the SM, DC machine and an encoder. The DSP controller and the power unit are also illustrated.

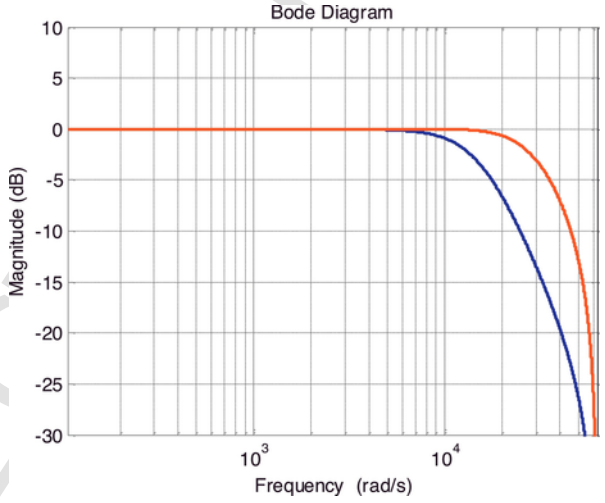

Fig. 10. System_5 (blue trace) and System_6 (red trace) close-loop frequency response. (For interpretation of the references to colour in this figure legend, the reader is referred to the web version of this article.)

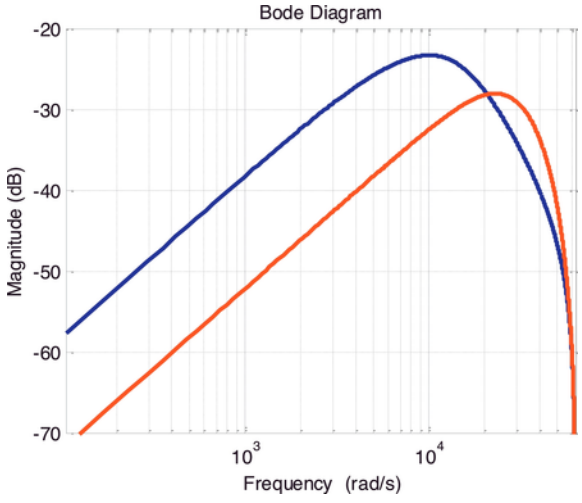

Fig. 11. System_5 (blue trace) and System_6 (red trace) frequency response in front of a perturbation. (For interpretation of the references to colour in this figure legend, the reader is referred to the web version of this article.)

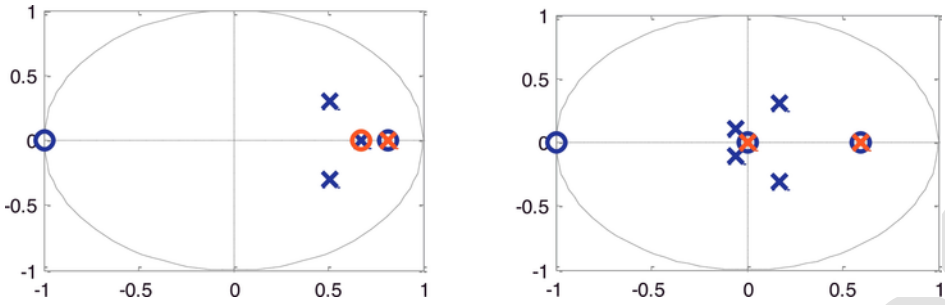

Fig. 12. Pole zero map for System_5 (left) and System_6 (right). In blue the poles and zeros of the close-loop systems and in red the poles and zeros of the PFs. (For interpretation of the references to colour in this figure legend, the reader is referred to the web version of this article.)

Assuming a back EMF of 50 V, it would create against the 4.2 A of the nominal phase current, an unwanted sinusoidal current of 2.95 A and 0.76 A for System_5 and System_6, respectively. This numerical example proves the superior back EMF rejection capability of System_6.

Fig. 12 plots the pole zero map for systems 5 and 6. In blue the poles and zeros of the close-loop systems and in red the poles and zeros of the PF. System_6 pole zero map is consistent with Table 2. Notice how the zero placed at (−0.993 + 0i) is not compensated by the PF as justified in Section 6.

8.1. Speed steps response

Fig. 13 plots the encoder measured position response (upper traces) of the three systems when the speed reference (lower trace) has been continuously increased with steps of 120 rpm (i.e. 100 Hz for the current frequency). The three systems involved are the two previously described and an additional System _6 with the same BW as the PI (i.e. $Ts_{2\%} = 400$ µs).

It is clearly illustrated how System_5 (blue upper trace) is the first of not being able to track the speed at 1200 rpm (i.e. 1000 Hz). This lack of trackability is manifested because the measured position does not increase as it should. Actually, the SM is losing steps.

System _6 (red upper trace) with the same BW as the PI (i.e. $Ts_{2\%} = 400$ µs) has been included for comparative reasons. Such system is able to track the demanded speed up to 1440 rpm and loses the tracking capability at 1560 rpm (i.e. 1300 Hz).

Finally, when the BW of System_6 is increased towards its maximum, the speed tracking capability still exits at 1800 rpm (i.e. 1500 Hz), as it can be clearly seen in the green upper trace of Fig. 13.

Such comparison not only experimentally proves that at the same BW the new controller tracking capability is superior to the PI one, but also demonstrates how the new controller can enlarge its BW without losing stability and therefore increasing the maximum speed.

8.2. Speed reversal trapezoidal profile

A widely common test for electrical machines speed controllers is the speed reversal following a trapezoidal speed profile, which implies that the position follows a second order polynomial waveform.

Such test compares System_5 ($Ts_{2\%} = 400$ µs) and System_6 ($Ts_{2\%} = 200$ µs), both at its maximum BW. To fully show both controllers' performance, the magnitudes illustrated are the measured current (just one axis), the speed reference and the reference and measured positions.

It should be noticed firstly, how the speed ramp is so steep, achieving the final speed in less than 20 ms and secondly how the speed reversal test includes both positive and negative speeds.

Final value of the speed ramp is 900 rpm (i.e. 750 Hz for the current frequency) for Figs. 14 and 15, 1080 rpm (i.e. 900 Hz) for Figs. 16 and 17 and 1320 rpm (i.e. 1100 Hz) for Fig. 18.

Similarly as in the previous section, it is clearly proved that System_6 has a larger BW than System_5, since the former is still able to track 1320 rpm, as it is illustrated in Fig. 18, meanwhile the latter loses the tracking capability at 1080 rpm, as it is shown in Fig. 16. Such waste of speed trackability can be seen very clearly in Fig. 16

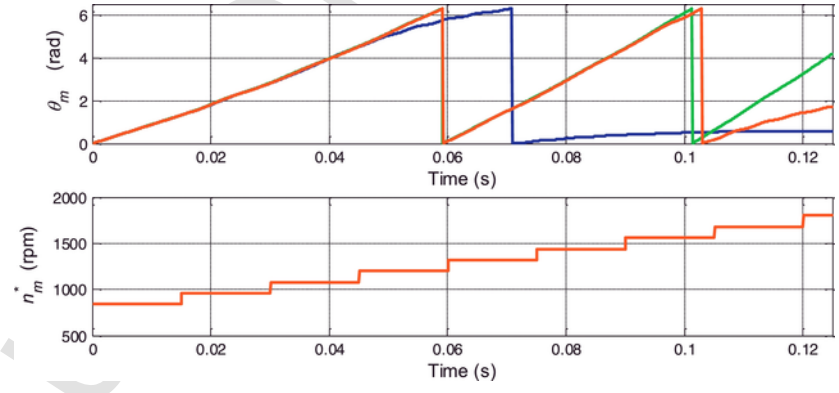

Fig. 13. Experimental speed steps response of System_5 (PI) and System_6 (new controller). It is illustrated the superior speed tracking capability of the proposed System_6. Top: measured position. Blue trace System_5 with $Ts_{2\%} = 400$ µs. Red trace System_6 with $Ts_{2\%} = 400$ µs. Green trace System_6 with $Ts_{2\%} = 200$ µs. Bottom: speed reference for the three systems with step increments of 120 rpm (i.e. 100 Hz). (For interpretation of the references to colour in this figure legend, the reader is referred to the web version of this article.)

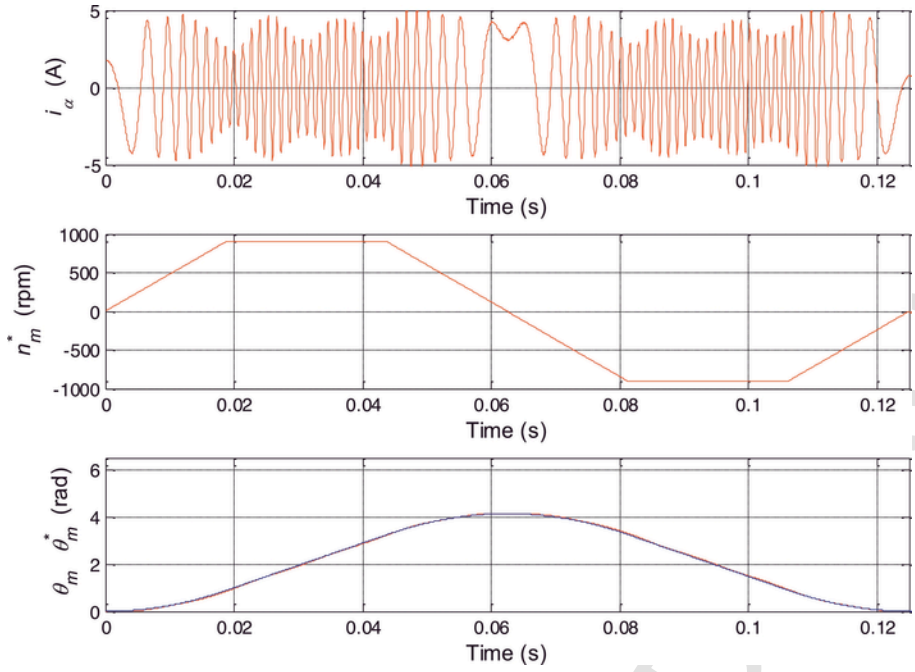

Fig. 14. Speed reversal ramp profile from zero, up to +900 rpm, down to −900 rpm and back to zero for System_5 (PI). From top to bottom: alpha measured current, speed reference and reference and measured positions.

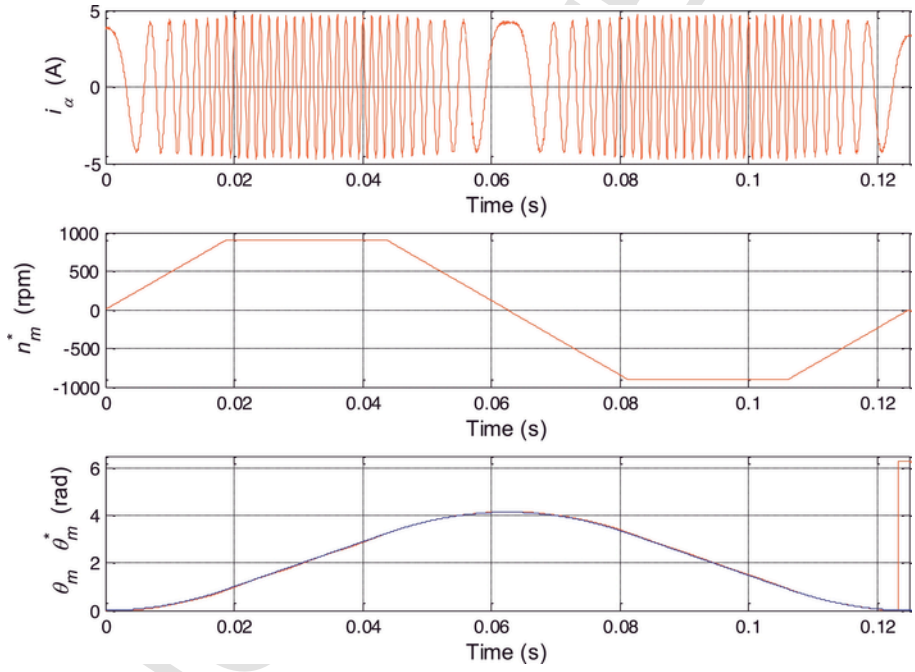

Fig. 15. Speed reversal ramp profile from zero, up to +900 rpm, down to −900 rpm and back to zero for System_6 (new controller). From top to bottom: alpha measured current, speed reference and reference and measured positions.

bottom trace, where the symmetry in the measured position waveform is lost because the SM is losing steps.

As a conclusion, it should be pointed that the new controller has increased the BW, according to Table 2, up to 4766 Hz, which is much further away than the experimental results shown in Sections 8.1 (1500 Hz, i.e. 1800 rpm) and 8.2 (1100 Hz, i.e. 1320 rpm). With the new design proposed, the BW is no longer the limitation for mounting in speed. Still, however, the there are two main reasons for not going higher in frequency and both of them are due to the back EMF.

The first reason is that at high speeds, large back EMF needs to be cancelled and consequently greater voltages are required. Actually, when the maximum DC voltage is reached, the current loop saturates and the anti-windup is activated, causing a current distortion and challenging the tracking capability.

The second reason is the limited back EMF rejection capability, as it was previously discussed with the help of Fig. 11. The detail pro-

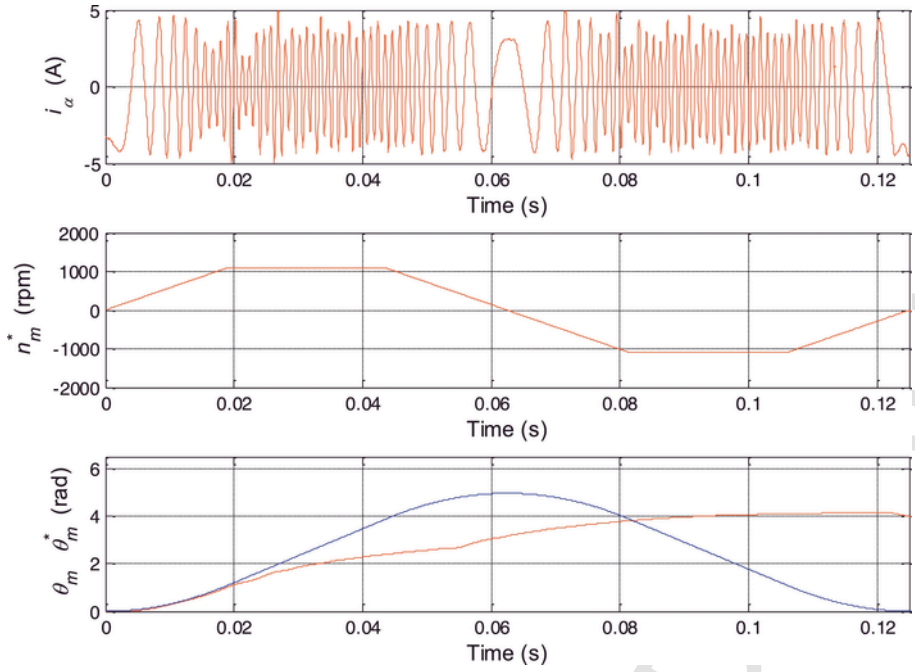

Fig. 16. Speed reversal ramp profile from zero, up to +1080 rpm, down to −1080 rpm and back to zero for System_5 (PI). From top to bottom: alpha measured current, speed reference and reference and measured positions.

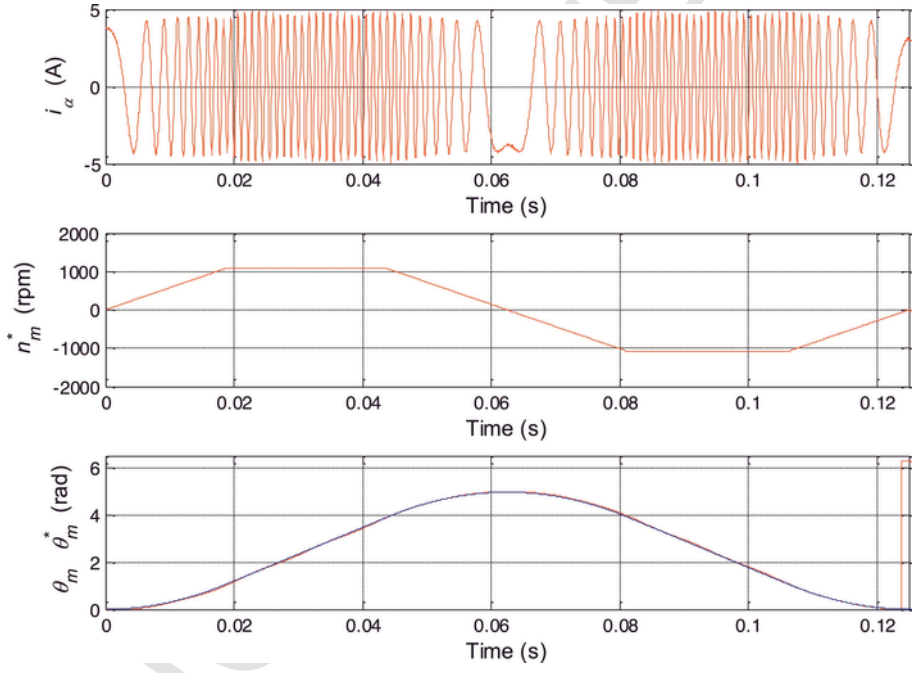

Fig. 17. Speed reversal ramp profile from zero, up to +1080 rpm, down to −1080 rpm and back to zero for System_6 (new controller). From top to bottom: alpha measured current, speed reference and reference and measured positions.

vided in Fig. 19 illustrates how the measured current is phase shifted from the reference one, despite being inside the BW (1080 rpm, i.e. 900 Hz). This lack of entire back EMF cancellation, which worsens at higher speeds, is the main cause of such current phase shift. At lower speeds, the current tracking is almost perfect, as it can be seen in Fig. 20. Such phase shifts, nevertheless, does not compromise the torque developed by the SM, since it affects at the same time and manner both alpha and beta current components.

8.3. Load impact at constant speed

The third experiment involves a load impact test when the speed reference is set at 540 rpm. Such external load torque has been introduced by the DC machine of the workbench, which is illustrated in Fig. 9. In Fig. 21, the top signal is the measured alpha current which is undisturbed when the load impact is applied at 0.02 s according to

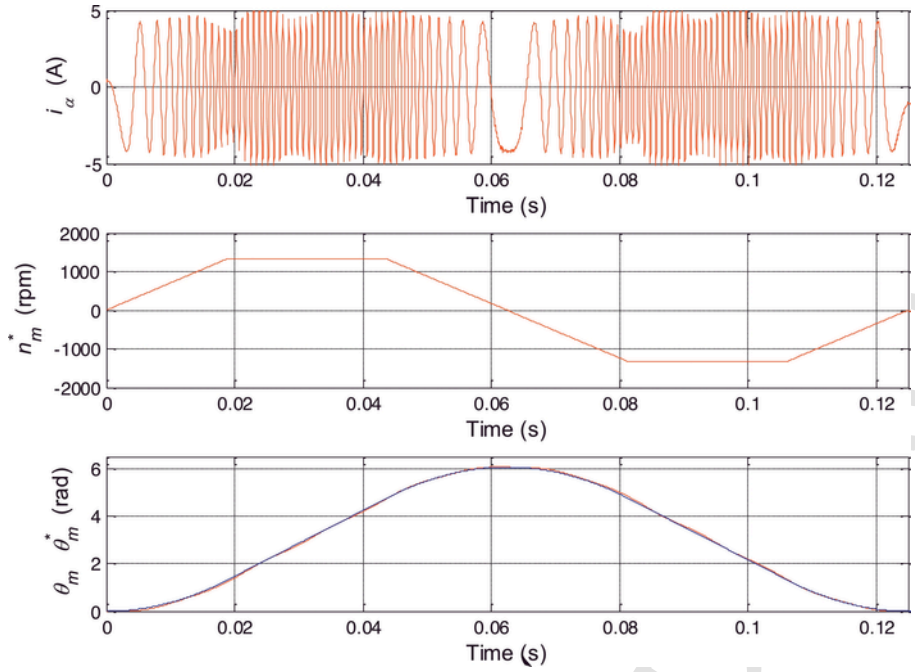

Fig. 18. Speed reversal ramp profile from zero, up to +1320 rpm, down to −1320 rpm and back to zero for System_6 (new controller). From top to bottom: alpha measured current, speed reference and reference and measured positions.

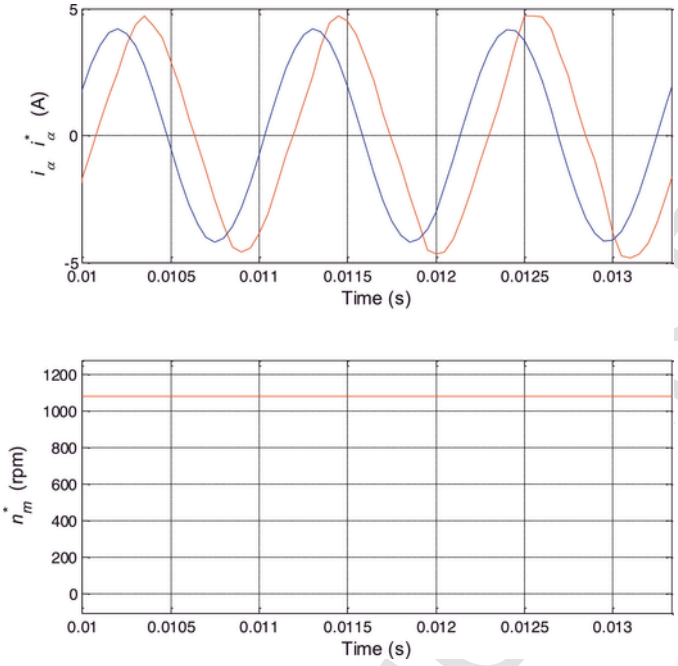

Fig. 19. Current loop performance at high speed (1080 rpm, i.e. 900 Hz). Top: alpha axis set point (blue) and actual (red) currents. Bottom: speed reference. (For interpretation of the references to colour in this figure legend, the reader is referred to the web version of this article.)

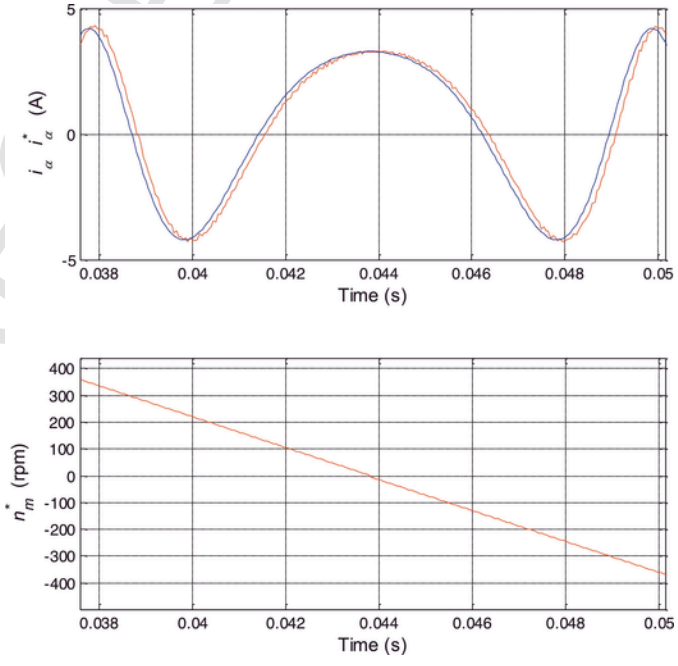

Fig. 20. Current loop performance at low speed. Top: alpha axis set point (blue) and actual (red) currents. Bottom: speed reference. (For interpretation of the references to colour in this figure legend, the reader is referred to the web version of this article.)

the bottom waveform. The point of the middle waveform is to prove the load application. It shows the subtraction between the angle of the vector current (workout from the measured alpha and beta currents) and the angle measured from the encoder (which is somehow the permanent magnet angle). From Eq. (3), it can be concluded that the angle between the permanent magnet vector and the current vector regulates the electromechanical torque developed by the SM [2].

Therefore, it is experimentally proved the capability of the new algorithm to cope with sudden load torque variations.

9. Industry prototype

This new controller has been applied in an industry 2 axis rapid prototyping Printed Circuit Boards (PCBs) machine [26], which is illustrated in the picture of Fig. 22. Such milling PCB machine is the

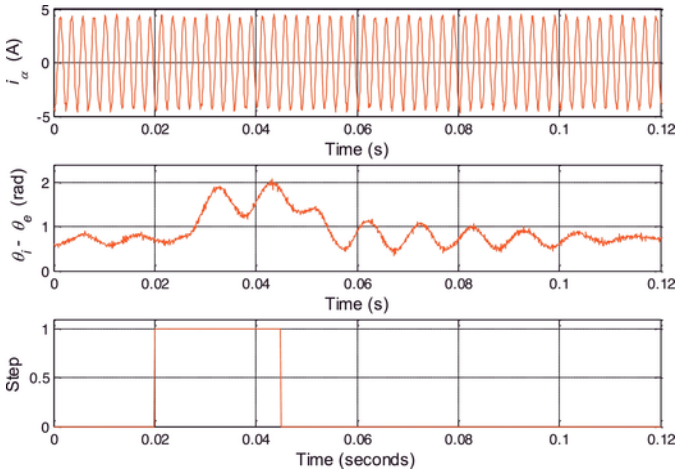

Fig. 21. Load impact at 540 rpm. Top: alpha axis measured current. Middle: difference between the measured current angle and the encoder measured angle. Bottom: load torque impact signal.

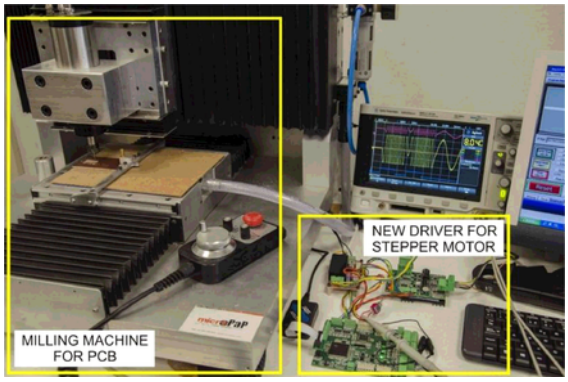

Fig. 22. Industry 2 axis rapid prototyping Printed Circuit Boards (PCBs) milling machine.

fruitful collaboration between the University and a private company and it is a tangible example of how increasing the SM speed reduces the time employed for rapid prototyping.

Currently, such novel high BW SM based drive is being implemented in a labeling machine for a wine manufacturer and it is expected that it will implemented in more industry applications where the rapidity is a key issue.

10. Conclusions

High speed is one of the challenges of Stepping motors (SM) for industry based motor drives. In this work, it has been maximised the achievable speed when using SM drives in order to try to compete with other encoder feedback based AC motor drives.

Initially, this work has justified why traditional PI controllers are not sufficient to achieve high dynamics drives when using SM. Instead an accurate model of the SM drive, with all existing delays, has been obtained in order to design a pole placement discrete-time domain controller with a high bandwidth.

A first set of experimental results, obtained in a University based laboratory workbench, has been reported. Speed reversal trapezoidal profile up to 1320 rpm and load impact experimental tests and waveforms are fully reported. Even a maximum speed of 1800 rpm has been achieved and illustrated.

It can be concluded that with the new proposed design, the closed-loop BW is no longer the limitation for mounting in speed.

Finally, a real 2 axis rapid prototyping Printed Circuit Boards machine has been designed and commercialised by an industry, which is a tangible example of how increasing the SM speed reduces the time employed for rapid prototyping.

Acknowledgements

The authors would like to acknowledge the Spanish research project DPI2013-41224-P (Ministerio de Educación) and the Catalan research project 2014 SGR 267 (AGAUR).

Appendix. List of symbols

Stepper motor variables

v_i ; $i = \{\alpha, \beta\}$	(V) Voltage per phase
i_i ; $i = \{\alpha, \beta\}$	(A) Current per phase
R	(Ω) Stator resistance per phase
L	(H) Inductance per phase
θ_e	(rad) Electrical angle from the encoder
θ_m	(rad) Mechanical angle from the encoder
θ_i	(rad) Electrical angle from the measured currents
Ψ_{PM}	(Wb) Permanent magnet flux
ω_e	(rad/s) Electrical angular speed
ω_m	(rad/s) Mechanical angular speed
n_m	(rpm) Mechanical angular speed
T_e	(N·m) Electromechanical torque
Nr	Rotor Pole number

Other variables

T_{PWM}	(s) Pulse width modulation period
T	(s) Sampling period
F_S	(Hz) Sampling frequency
$Ts_{2\%}$	(s) Settling time at 2%
ζ	Damping factor of a second-order system
ω_n	(rad/s) Natural frequency of a second-order system
J	(Kg·m^2) Total moment of inertia
F	(N·m·s/rad) Total friction coefficient
T_L	(N·m) External load torque

Operators

s	Laplace operator
z	Z transform operator

Axis reference frames

α/β	Two-phase orthogonal stationary frame

References

[1] T Kenjo, A Sugawara, Stepping motors and their microprocessor controls, Oxford University Press, 1994.
[2] P Acarnley, Stepping motors: a guide to theory and practice, The Institution of Electrical Engineers, 2002.
[3] H Zhu, Y Feng, P Yang, Auto-scanning and visualizing system for the acoustic field of transducer, Rob Comput-Integr Manuf 28 (2012) 631–636.
[4] Z Dong, Nonlinear power-level control design for MHTGRs by considering stepper motor dynamics, Prog Nucl Energy 78 (2015) 216–230.
[5] DS Milutinovic, R Sato, D Matsuura, K Ehmann, Mechanism for active Π-joint as an equivalent to the combination of revolute joint and proximal fixed-length link, Rob Comput-Integr Manuf (2015).

[6] C Gradl, A Plöckinger, R Scheidl, Sensorless position control with a hydraulic stepper drive — concept, compression modeling and experimental investigation, Mechatron 35 (2016) 91–101.
[7] BK Bose, Power electronics and motor drives, Elsevier/Academic Press, 2006.
[8] K Wonhee, Y Chuan, C Chung Choo, Design and implementation of simple field-oriented control for permanent magnet stepper motors without DQ transformation, Magn IEEE Trans 47 (2011) 4231–4234.
[9] K Wonhee, S Donghoon, C Chung Choo, Microstepping with nonlinear torque modulation for permanent magnet stepper motors, Control systTechnol IEEE Trans 21 (2013) 1971–1979.
[10] S Moon, DH Kim, Step-out detection and error compensation for a micro-stepper motor using current feedback, Mechatron 24 (2014) 265–273.
[11] K Balakrishnan, B Umamaheswari, K Latha, Identification of resonance in hybrid stepper motor through measured current dynamics in online for accurate position estimation and control, Ind Inf IEEE Trans 9 (2013) 1056–1063.
[12] M Bendjedia, Y Ait-Amirat, B Walther, A Berthon, Position control of a sensorless stepper motor, Power Electron IEEE Trans 27 (2012) 578–587.
[13] M Butcher, A Masi, R Picatoste, A Giustiniani, Hybrid stepper motor electrical model extensions for use in intelligent drives, Ind Electron IEEE Trans 61 (2014) 917–929.
[14] W Kim, D Shin, CC Chung, The Lyapunov-based controller with a passive nonlinear observer to improve position tracking performance of microstepping in permanent magnet stepper motors, Autom 48 (2012) 3064–3074.
[15] S Donghoon, K Wonhee, L Youngwoo, C Chung Choo, Phase-compensated microstepping for permanent-magnet stepper motors, Ind Electron IEEE Trans 60 (2013) 5773–5780.
[16] K Wonhee, C Chung Choo, Novel position detection method for permanent magnet stepper motors using only current feedback, Magn IEEE Trans 47 (2011) 3590–3593.
[17] K Wonhee, S Donghoon, C Chung Choo, Microstepping using a disturbance observer and a variable structure controller for permanent-magnet stepper motors, Ind Electron IEEE Trans 60 (2013) 2689–2699.
[18] W. Kim, D. Shin, Y Lee, CC Chung, Simplified torque modulated microstepping for position control of permanent magnet stepper motors, Mechatron 35 (2016) 162–172.
[19] S Rustemli, M Yilmaz, M Demirtas, Ripple reduction at speed and torque of step motors used on a two-axis robot arm, Rob Comput-Integr Manuf 26 (2010) 759–767.
[20] SE Lyshevski, Microstepping and high-performance control of permanent-magnet stepper motors, Energy Convers Manage 85 (2014) 245–253.
[21] HM Hasanien, FPGA implementation of adaptive ANN controller for speed regulation of permanent magnet stepper motor drives, Energy Convers Manage 52 (2011) 1252–1257.
[22] L Quy Ngoc, J Jae-Wook, Neural-network-based low-speed-damping controller for stepper motor with an FPGA, Ind Electron IEEE Trans 57 (2010) 3167–3180.
[23] M Heertjes, T Oomen, D Trumper, Introduction to the special issue on control of high-precision motion systems, Mechatron 24 (2014) 547–548.
[24] BGB Hunnekens, MF Heertjes, N van de Wouw, H. Nijmeijer, Performance optimization of piecewise affine variable-gain controllers for linear motion systems, Mechatron 24 (2014) 648–660.
[25] YR Teo, D Russell, SS Aphale, AJ Fleming, Optimal integral force feedback and structured PI tracking control: application for objective lens positioner, Mechatron 24 (2014) 701–711.
[26] MICROPAP_EASY_MOTION, http://www.micropap.com/index.php/blog/electronica/item/16-presentacion-cnc.
[27] NSS Mar, PKDV Yarlagadda, C Fookes, Design and development of automatic visual inspection system for PCB manufacturing, Rob Comput-Integra Manuf 27 (2011) 949–962.
[28] S Vongbunyong, S Kara, M Pagnucco, Learning and revision in cognitive robotics disassembly automation, Rob Comput-Integr Manuf 34 (2015) 79–94.
[29] M Iwasaki, K Seki, Y Maeda, High-precision motion control techniques: a promising approach to improving motion performance, Ind Electron Mag IEEE 6 (2012) 32–40.
[30] CL Phillips, HT Nagle, Digital control system, 3rd ed, Person Education International Inc, 1998.
[31] C-T Chen, Linear system theory and design, Oxford University Press, 2014.
[32] K Ogata, Modern control engineering, 5th International Edition ed., Pearson, 2010.
[33] P Hippe, Windup in control. Its effects and their prevention, Springer, 2006.
[34] C Jong-Woo, L Sang-Cheol, Antiwindup strategy for PI-type speed controller, Ind Electron IEEE Trans 56 (2009) 2039–2046.
[35] T Instruments, http://www.ti.com/product/tms320f28335.
[36] N Mohan, Electric machines and drives: a first course, Wiley, 2012.

Antoni Arias received the BEng degree in electrical engineering, MEng and PhD degrees in control and electronic engineering from the *Universitat Politècnica de Catalunya*, Catalonia, Spain, in 1993, 1997 and 2001 respectively. From 1992 to 1995 he worked at *SADECT S.A.,* a local industrial electronics company. Since 1996 he has been a Lecturer at the *Universitat Politècnica de Catalunya* and was appointed as an Associate Professor in 2002 at the same University. In 1999 he was a visiting research assistant and part time lecturer at the University of Glamorgan, UK. In 2003 and 2004 he joined as a Visiting Fellow the Power Electronics, Machines and Control Group at the University of Nottingham, UK. In 2011 and 2012 he was at the *Laboratoire de Génie Electrique de Paris* (France) as a *Maître de Conférences invité*. His research interests include sensorless variable-speed drive systems, power electronics converters and control strategies.

Jesús Caum received the BEng degree in electrical engineering, MEng in control and electronic engineering and PhD degrees in optics engineering from the *Universitat Politècnica de Catalunya (UPC)*, Catalonia, Spain, in 1987, 1998 and 2010 respectively. Since 1987 he has been a Lecturer at the *Universitat Politècnica de Catalunya* and was appointed as an Associate Professor in 1992 at the same University. He is a member of the CD6 (Centre Development Sensors and Systems UPC) since 1995. His research interests include design conditioning circuits for sensors electro optics and electronics and control strategies applied a stepper motors.

Robert Griñó received the M.Sc. degree in electrical engineering and the Ph.D. degree in automatic control from the Universitat

Politècnica de Catalunya (UPC), Barcelona, Spain, in 1989 and 1997, respectively. From 1990 to 1991, he was a Research Assistant with the Instituto de Cibernètica, UPC. From 1992 to 1998, he was an Assistant Professor with the Automatic Control Department, Universitat Politècnica de Catalunya, where he has been an Associate Professor since 1998. His research interests include digital control, nonlinear control, stability theory and control of power electronics converters. Dr. Griñó is a senior member of IEEE and a member of the Spanish Society on Automation and Control-IFAC.